




RESEARCH ARTICLE | JULY 03 2025

Thermodynamic principles for optimizing multi-junction photovoltaics—Exemplified for perovskite-based indoor photovoltaics ^{EP}

Special Collection: [Novel Simulation Approaches of Perovskite Optoelectronic Devices and Materials](#)Austin M. Kay  ; Drew B. Riley  ; Gregory Burwell  ; Paul Meredith  

APL Energy 3, 036102 (2025)

<https://doi.org/10.1063/5.0266374>

Articles You May Be Interested In

Anticorrelated photoluminescence and free charge generation proves field-assisted exciton dissociation in low-offset PM6:Y5 organic solar cells

APL Mater. (June 2023)

Relationship between charge transfer state electroluminescence and the degradation of organic photovoltaics

Appl. Phys. Lett. (February 2021)

Polycrystalline thin-film CdS liquid junction photovoltaic cell

J. Appl. Phys. (January 1980)



Special Topics Open for Submissions

[Learn More](#)

Thermodynamic principles for optimizing multi-junction photovoltaics—Exemplified for perovskite-based indoor photovoltaics

Cite as: APL Energy 3, 036102 (2025); doi: [10.1063/5.0266374](https://doi.org/10.1063/5.0266374)

Submitted: 18 February 2025 • Accepted: 19 June 2025 •

Published Online: 3 July 2025



Austin M. Kay,^{a)}  Drew B. Riley,^{b)}  Gregory Burwell,^{b)}  and Paul Meredith^{b)} 

AFFILIATIONS

Sustainable Advanced Materials Group (Sêr-SAM), Centre for Integrative Semiconductor Materials (CISM), Department of Physics, Swansea University Bay Campus, Swansea SA1 8EN, United Kingdom

Note: This paper is part of the Special Topic on Novel Simulation Approaches of Perovskite Optoelectronic Devices and Materials.

^{a)} Email: a.m.kay.954708@swansea.ac.uk

^{b)} Author to whom correspondence should be addressed: paul.meredith@swansea.ac.uk

ABSTRACT

Multi-junction architectures are utilized in photovoltaic (PV) technology to widen spectral range, increase voltage and/or current, and hence deliver higher overall power conversion efficiencies (PCEs). However, accurate approaches for simulating multi-junction PVs using the electro-optical properties of real materials are somewhat scarce—particularly in the context of novel applications such as indoor PVs, where the illumination spectrum differs from natural sunlight. Herein, we present a robust methodology—alongside an open-source simulation tool—for modeling multi-junction PVs while accounting for intrinsic PV features, including sub-gap absorption, band-filling effects, and radiative couplings between junctions. Although we primarily focus our investigation on perovskite-based multi-junction devices, our approach is extendable to any class of PV material. We apply it in the context of indoor PVs by assuming the LED-B4 spectrum as a representative light source. At a typical illuminance of 1000 lux, we find that PCEs above 60% are possible by combining a 2.1 eV wide-gap top cell with a 1.0–2.0 eV narrow-gap bottom cell, meaning that a suitable wide-gap semiconductor could be coupled with almost any conventional solar cell to achieve high performance. Using the spectral responses of real PV devices, we then predict optimal material configurations under LED-B4 illumination, before probing the spectral versatility of these devices under a variety of indoor light sources and intensities. We find that the maximum power point voltage is mostly independent of light source, while PCE is more sensitive due to changes in current density, which provides insight into how laboratory-optimized devices may perform in realistic scenarios.

© 2025 Author(s). All article content, except where otherwise noted, is licensed under a Creative Commons Attribution (CC BY) license (<https://creativecommons.org/licenses/by/4.0/>). <https://doi.org/10.1063/5.0266374>

I. INTRODUCTION

Utilizing two or more semiconductor materials of varying bandgap energy (E_g), multi-junction photovoltaics (PVs) can harvest photons from a wider spectral range while reducing thermalization losses when compared with single-junction PVs.^{1–3} This, in turn, leads to improvements in open-circuit voltage (V_{oc}), maximum power point voltage (V_{mpp}), and power conversion efficiency (PCE).⁴ However, these improvements come with a caveat: the total current produced by the multi-junction device is limited by the smallest current of any given junction when connected in series, so these currents must be closely matched to avoid additional recombination losses at the junction interface.^{5,6} This problem has a

non-trivial solution that is generally based on a delicate optimization of the optical, electronic, and physical properties of each cell in the multi-junction device. Several techniques are currently available to optimize the design of multi-junction PVs, including analytical approaches,^{7–9} optical approaches,¹⁰ tunnel-junction models,^{11,12} and multi-scale electro-optical device models such as Solcore and SETFOS.^{13–15} While each approach has its merits, there is often a trade-off between enhanced accuracy (arising from increased simulation complexity) and computational expense/simulation time.¹⁶

Historically, multi-junction device modeling has mainly been focused on devices composed of high-value and precisely engineered III–V semiconductor materials,^{17–19} with an emphasis on space and solar concentrator applications.^{20–23} More recently, multi-junctions

have been considered in the context of perovskite-based tandems for terrestrial applications (i.e., under AM1.5 G illumination).^{24–26} Often (although not always), device models account for the emission and absorption of light between cells of the multi-junction device—known as radiative coupling—although it is assumed to occur unidirectionally from the top cell (which the incident light hits first) to the bottom cell, as the former typically has the wider bandgap.²⁴ However, for systems with complex emission and absorption properties, light emitted by the bottom cell could also be absorbed by the top cell. These properties include sub-gap absorption induced by trap states and energetic disorder,^{27–30} with exponentially decaying sub-gap absorption—known as an Urbach tail—being conspicuous near the bandgap in most semiconductor materials, including perovskites, organics, and cadmium telluride (CdTe).^{31–36} Importantly, as the occupancies of these sub-gap states change under an applied voltage bias through a process known as band-filling, they can influence the V_{oc} and PCE of the device.^{37,38} Understanding the absorption properties of these states can therefore provide valuable insight into device performance, with measurement techniques such as ultra-sensitive external quantum efficiency (us-EQE_{PV}), Fourier transform photocurrent spectroscopy, and photothermal deflection spectroscopy (PDS) being particularly useful.^{39–45}

In this work, we present a general method alongside an open-source computational tool⁴⁶ for simulating the performance of multi-junction PVs under an arbitrary light source and intensity. Utilizing the photovoltaic external quantum efficiency (EQE_{PV}) and one-sun open-circuit voltage of individual cells of the multi-junction device, our approach predicts power generation parameters while accounting for band-filling, sub-gap absorption, non-radiative open-circuit voltage losses, and realistic bidirectional radiative coupling. We apply this analysis to a test case: perovskite-based multi-junction devices for indoor PV applications. In recent years, a multitude of wide-gap perovskites has been developed in the pursuit of high-efficiency perovskite–perovskite and perovskite–silicon AM1.5 tandems,^{47,48} with a wealth of experimental measurements waiting to be recontextualized for novel applications. Indeed, many of these wider-gap systems may be well-suited to indoor PV applications.^{49,50} Although we focused our investigation on perovskite-based indoor PVs, the simulation approach is applicable to any semiconductor material and illumination condition. We present simulations of the performance of different combinations of perovskite–perovskite and perovskite–inorganic PVs under conditions specified in indoor PV testing standard IEC TS 62607-7-2:2023.^{51,52} We conclude by considering how these same PVs perform under a variety of typical indoor lighting conditions, which demonstrates that our approach gives insight into how a testing standard-optimized device may perform in some of the diverse illumination conditions commonly found indoors.

II. RESULTS AND DISCUSSION

A. Thermodynamic limit of single-junction photovoltaics

The current–voltage characteristics of a single-junction PV device can be described using the ideal diode equation, which relates the current density (J) to the applied voltage (V) through¹

$$J(V) = J_0(V) \left[\exp \left(\frac{qV}{k_B T} \right) - 1 \right] + \frac{V}{R_{sh}} - J_{ph}(V), \quad (1)$$

where q is the elementary charge, k_B is the Boltzmann constant, T is the temperature, and R_{sh} is the shunt resistance. A full list of symbols and abbreviations is provided as [supplementary material](#) (Note 1). The spectral response of the device enters Eq. (1) via the calculation of the photocurrent density (J_{ph}) and the dark saturation current density (J_0). The former can be calculated by combining the measured photovoltaic external quantum efficiency (EQE_{PV}) with the photon flux of the light source (Φ_{source}) using³⁸

$$J_{ph}(V) = q \int_0^\infty EQE_{PV}(E) \tanh \left(\frac{E - qV}{4k_B T} \right) \Phi_{source}(E) dE, \quad (2)$$

where E denotes the photon energy. The hyperbolic term in this expression accounts for band-filling effects in materials with a disordered density-of-states.³⁸ On the other hand, the dark saturation current density can be defined through reciprocity in terms of the electroluminescent external quantum efficiency (EQE_{EL}) as^{37,53}

$$J_0(V) = \frac{q}{EQE_{EL}} \int_0^\infty EQE_{PV}(E) w(E, V) \Phi_{Planck}(E) dE, \quad (3)$$

where $\Phi_{Planck}(E) = \frac{2\pi E^2}{h^3 c^2} \left[\exp \left(\frac{E}{k_B T} \right) - 1 \right]^{-1}$ is the photon flux of thermal radiation for a cell at temperature T , with h and c being the Planck constant and the speed of light in vacuum, respectively. The additional term (w) introduced in Eq. (3) is a correction factor that accounts for the combined effects of band-filling and the chemical potential of radiation;^{38,54} it may be written as³⁷

$$w(E, V) = \frac{1}{\left[1 + \exp \left(\frac{qV - E}{2k_B T} \right) \right]^2}. \quad (4)$$

We note that the series resistance of the device can also be incorporated into Eq. (1),¹ but its effect only becomes prominent at higher light intensities and is minimal for the low current densities typical of indoor PVs, as we discuss further in Sec. II E. The shunt resistance, on the other hand, plays a more pivotal role under the low-intensity illumination conditions found indoors.⁵⁵

To demonstrate how Eqs. (1)–(4) can be utilized to numerically predict the PCE of a single-junction PV device, we now present a case study using a double cation perovskite (DCP) device recently published by Othman *et al.*⁵⁶ Figure 1(a) shows the sensitive EQE_{PV} spectrum for this device, with the gray region indicating how the measurement becomes limited by thermal noise at low photon energies.⁴⁰ The blue region indicates the absorption features of deep trap states.⁵⁶ Note that optical interference between incident and back-reflected light within the thin-film device can affect the line shape of the EQE_{PV} spectrum in this region.^{57–59} Finally, the green region above $E_g = 1.53$ eV (identified from the maximal rate of change in EQE_{PV}) indicates where band-to-band transitions occur. Between the blue and green regions, broadening of the band edges by energetic disorder leads to the formation of an Urbach tail, in which the sub-gap EQE_{PV} grows exponentially.^{27,28,30} Generally, this sub-gap EQE_{PV} leads to a lower PCE by reducing a device's V_{oc} and V_{mpp} .³⁷ It can also lead to ideality factors greater than one (see [supplementary material](#) - Note 2).³⁰

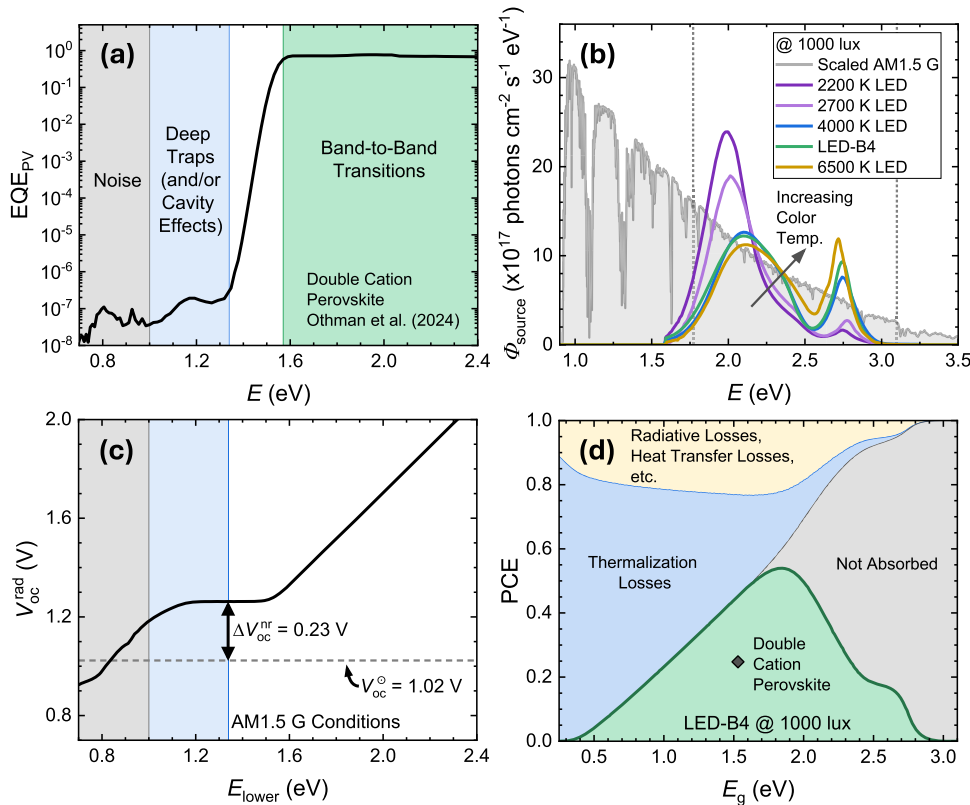


FIG. 1. Evaluating single-junction PV performance using photovoltaic external quantum efficiency (EQE_{PV}) measurements. **(a)** EQE_{PV} spectrum of a double cation perovskite (DCP) device,⁵⁶ with the noise-limited, trap-limited, and above-gap regions indicated in gray, blue, and green, respectively. Between the blue and green regions, EQE_{PV} grows exponentially through an Urbach tail. **(b)** Photon flux (Φ_{source}) of typical LEDs, plotted at an illuminance of 1000 lux as a function of the photon energy (E). Note that the visible light region is bounded by vertical dotted lines. For reference, the AM1.5 G spectrum is included and scaled to 1000 lux. **(c)** Radiative open-circuit voltage (V_{oc}^{rad}) of the DCP device under AM1.5 G illumination, calculated using Eqs. (1)–(4) and then plotted vs the lower limit of the integral (E_{lower}). The open-circuit voltage determined experimentally under AM1.5 G conditions (V_{oc}^{exp} = 1.02 V) is indicated by the dashed line, with the difference between the two indicating the non-radiative open-circuit voltage loss (ΔV_{oc}^{nr}). **(d)** PCE of the DCP device under LED-B4 illumination (black diamond), plotted alongside PCEs and losses vs bandgap (E_g) in the Shockley–Queisser model.

By combining its EQE_{PV} spectrum with a known photon flux, the performance of the DCP device (or indeed any PV device) can be simulated under any set of illumination conditions using Eqs. (1)–(4). Figure 1(b) shows the photon fluxes of exemplary LED light sources with a variety of color temperatures, with the green line indicating the (CIE standard illuminant) LED-B4 spectrum specified in indoor PV testing standard IEC TS 62607-7-2:2023.^{51,52} As this investigation was focused on indoor applications of multi-junction PVs, an irradiance of 0.3132 mW cm⁻² (corresponding to an illuminance of 1000 lux) was assumed as representative of a well-lit room,⁶⁰ with all spectra in Fig. 1(b) being scaled to 1000 lux by combining the photon flux in the visible region with the photopic response of the human eye (see [supplementary material](#) - Note 3 for more details).⁶¹ For reference, a version of the AM1.5 G solar spectrum scaled to 1000 lux (or, equally, an irradiance of 0.865 mW cm⁻²) is also included, which is broader and redshifted relative to any of the LED spectra.

As not all features in the EQE_{PV} spectrum obey reciprocity or contribute to the thermodynamic limit,²⁹ the lower end of the EQE_{PV} spectrum must be truncated by introducing a lower bound (E_{lower} > 0) into the integrals of Eqs. (2) and (3). Figure 1(c) shows the results of this analysis, with the open-circuit voltage in the radiative limit (V_{oc}^{rad}) simulated under AM1.5 G conditions being plotted against the lower bound. Note that EQE_{EL} = 1 is assumed in Eq. (3) to give the radiative limit, while a cell temperature T = 293.15 K is assumed throughout this work. As E_{lower} decreases, more of the photon flux and device response are captured until the radiative

open-circuit voltage (V_{oc}^{rad}) reaches a plateau. As E_{lower} is further reduced, V_{oc}^{rad} continues to decrease due to the presence of deep trap states, ultimately dropping below the experimentally observed open-circuit voltage (V_{oc}^{exp} = 1.02 V; measured under AM1.5 G or one-sun conditions), which is indicated by the dashed line.⁵⁶ This non-physical result is due to deep trap states not being in thermodynamic equilibrium with charge-generating states, with their luminescence not being considered in the standard reciprocity theory and thus not contributing to the radiative thermodynamic limit.²⁹ So, in this case, EQE_{PV} below E_{lower} = 1.24 eV is removed. If a photovoltaic device's EQE_{PV} spectrum was not truncated in this way, then its simulated PCE would (incorrectly) be lower than its experimentally determined PCE.

By comparing V_{oc}^{rad} with V_{oc}^{exp} at the plateau in Fig. 1(c), the device's non-radiative open-circuit voltage loss can be estimated from measurements made under AM1.5 G conditions through ΔV_{oc}^{nr} ≈ V_{oc}^{rad} - V_{oc}^{exp} = 0.23 V. Assuming this value holds as a realistic estimate of the non-radiative loss under any set of illumination conditions,³⁷ then EQE_{EL} can be estimated using EQE_{EL} = exp(-qΔV_{oc}^{nr}/k_BT). The validity of this assumption is demonstrated in the [supplementary material](#) (Note 4).

With EQE_{EL} evaluated using the method described above, an upper estimate of the performance of the DCP device can be obtained under LED-B4 illumination. Figure 1(d) shows the resultant PCE of 24.1% alongside simulated Shockley–Queisser (SQ) limits. In the SQ model, EQE_{PV} is modeled as a step function—such

that all photons of energy $E \geq E_g$ are collected as electron-hole pairs (while photons of energy $E < E_g$ are not)—while recombination only occurs radiatively, giving $\text{EQE}_{\text{EL}} = 1$ and $\Delta V_{\text{oc}}^{\text{nr}} = 0$.⁶² The SQ model predicts a maximum PCE of around 54% under 1000 lux LED-B4 illumination, although this value can vary from one light source to another.^{63–65} For reference, the various loss pathways in the SQ model are illustrated, including losses from non-absorbed carriers (gray region), carrier thermalization (blue region), and radiative losses/energy transfer losses (yellow region);² see [supplementary material](#) (Note 5) for further details. By transitioning from single-junction to multi-junction devices, carrier thermalization losses can be reduced through the use of multiple bandgaps, whereas radiative losses can be reduced through radiative coupling between sub-cells, which effectively recycles emitted light.

B. Modeling multi-junction photovoltaics

We next consider the performance limits of a two-junction (or tandem) device. In practice, this approach is scalable to multi-junction devices with an arbitrary number of cells (see [supplementary material](#) - Note 6), but we limit our focus to two cells in the context of indoor PVs as the relevant photon fluxes are spectrally narrow compared to the solar spectrum. [Figure 2](#) shows a schematic of our approach (and analysis flow chart) to treating the two-junction architecture, with the absorption and emission of light by the two cells shown in [Fig. 2\(a\)](#). Notably, the two cells are connected in series, with the top cell's bandgap (E_g^1) usually being larger than the bottom cell's bandgap (E_g^2). In general, the current densities generated by each cell can be expressed as a modified form of Eq. (1),

$$J_1(V_1) = J_{0,1}(V_1) \left[\exp\left(\frac{qV_1}{k_B T}\right) - 1 \right] + \frac{V_1}{R_{\text{sh},1}} - J_{\text{ph},1}(V_1) - J_{2 \rightarrow 1}(V_1, V_{\text{em},2}), \quad (5a)$$

$$J_2(V_2) = J_{0,2}(V_2) \left[\exp\left(\frac{qV_2}{k_B T}\right) - 1 \right] + \frac{V_2}{R_{\text{sh},2}} - J_{\text{ph},2}(V_2) - J_{1 \rightarrow 2}(V_{\text{em},1}, V_2). \quad (5b)$$

Here, a 1 (2) in the sub-script indicates that the quantity is assigned to the top (bottom) cell. In these equations, the quantities $J_{1 \rightarrow 2}$ and $J_{2 \rightarrow 1}$ are the additional photocurrents generated in the bottom cell and top cell, respectively, due to emission from the other cell. These photocurrents arise due to radiative coupling and depend on the carrier densities under the relevant illumination conditions, which we approximate through the reciprocity principle using effective emission voltages $V_{\text{em},1}$ and $V_{\text{em},2}$, as we explore shortly. As before, a cell's EQE_{PV} spectrum enters these equations through the evaluation of the photocurrent and dark saturation current densities, which are determined using Eqs. (2) and (3), respectively. Each cell's EQE_{PV} spectrum is truncated using the technique described for a single-junction device in Sec. II A.

While the light incident on the top cell is simply given by $\Phi_1(E) = \Phi_{\text{source}}(E)$, only a fraction of this light will be transmitted through the top cell and onto the bottom cell. Neglecting reflective losses, the light incident on the bottom cell can be written as

$$\Phi_2(E) = \left[1 - \text{EQE}_{\text{PV},1}(E) \tanh\left(\frac{E - qV_1}{4k_B T}\right) \right] \Phi_{\text{source}}(E). \quad (6)$$

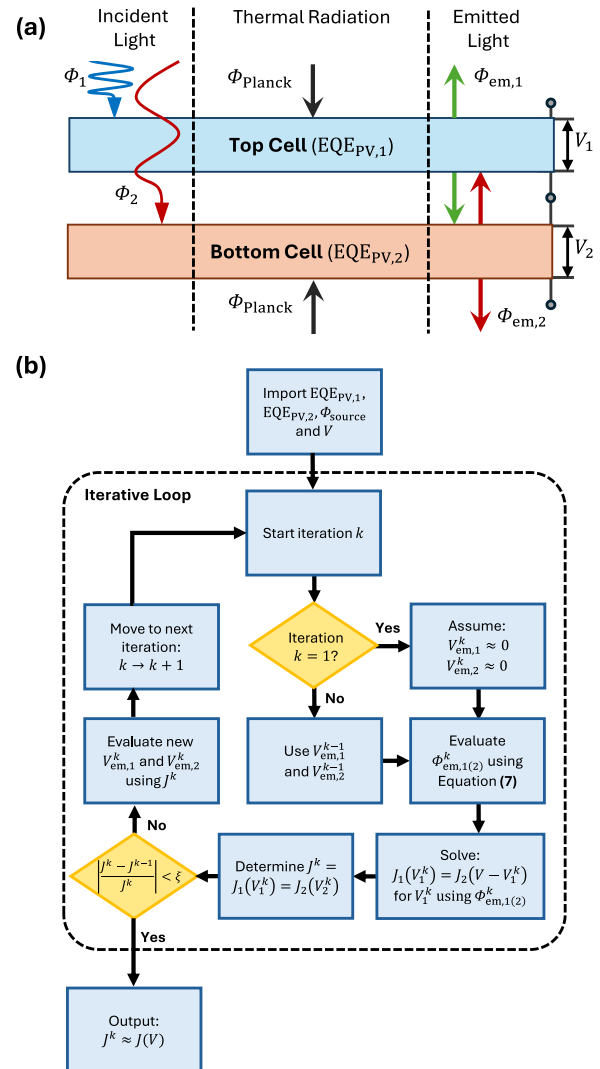


FIG. 2. (a) Schematic of the photon fluxes relevant to the modeling of a two-junction PV device. The light from the source is incident on the top cell ($\Phi_1 = \Phi_{\text{source}}$), while the light transmitted through it and onto the bottom cell (Φ_2) can be calculated using Eq. (6). In addition, the photon flux of thermal radiation (Φ_{Planck}) will also be absorbed by the device, leading to the thermal generation of charge carriers. Charge carriers undergo radiative recombination in both cells, leading to the emission of a photon flux from the top cell ($\Phi_{\text{em},1}$) and the bottom cell ($\Phi_{\text{em},2}$), which are calculated using Eq. (7). (b) Process flow chart for the iterative loop used to evaluate the total current J produced under voltage V while allowing for radiative coupling between cells, experimental EQE_{PV} spectra, non-radiative losses, band-filling effects, etc. Here, k denotes the iteration number and ξ the convergence criterion.

Note that a near-unity internal quantum efficiency (IQE) has been assumed in the top cell, such that $\text{EQE}_{\text{PV},1}$ approximates its absorbance. If the top cell's $\text{EQE}_{\text{PV},1}$ is reduced, it absorbs less light, leading to a larger Φ_2 incident on the bottom cell. This has implications for power generation, as we explore in Sec. II C.

To our knowledge, while unidirectional radiative coupling in the presence of sub-gap absorption has been explored in the past,²⁴ most approaches to model the thermodynamics of multi-junction PVs neglect radiative coupling from the narrower E_g bottom cell to the wider E_g top cell. This can be a reasonable assumption under solar conditions where the optimal bandgap configurations are energetically separated. However, as previously mentioned, this assumption neglects the absorption of sub-gap states, which are universally present in disordered semiconductor materials and contribute to the photocurrent.^{29,38} Accounting for bidirectional couplings also becomes more important under indoor illumination conditions as the narrower illumination spectra demand configurations of top and bottom cell materials that can be similar in E_g , as we explore in Sec. II C.

To quantify the radiative coupling between the cells of the multi-junction device, we utilize the reciprocity principle of a lone cell to evaluate its electroluminescent emission under given illumination conditions. First, the current density is evaluated utilizing Eq. (1); then, the effective voltage of emission required to drive the cell to the equivalent current density in the dark is evaluated—for cell m , this is labeled $V_{em,m}$. Following this, the electroluminescence spectrum of cell m can be evaluated through⁵³

$$\Phi_{em,m}(E, V_{em,m}) = \text{EQEPV},m(E) w(E, V_{em,m}) \times \Phi_{\text{Planck}}(E) \left[\exp\left(\frac{qV_{em,m}}{k_B T}\right) - 1 \right]. \quad (7)$$

The additional photocurrent arising from radiative coupling between cells may then be written as

$$J_{1 \rightarrow 2}(V_{em,1}, V_2) = \frac{q}{2} \int_0^\infty \text{EQEPV},2(E) \times \tanh\left(\frac{E - qV_2}{4k_B T}\right) \Phi_{em,1}(E, V_{em,1}) dE, \quad (8a)$$

$$J_{2 \rightarrow 1}(V_1, V_{em,2}) = \frac{q}{2} \int_0^\infty \text{EQEPV},1(E) \times \tanh\left(\frac{E - qV_1}{4k_B T}\right) \Phi_{em,2}(E, V_{em,2}) dE. \quad (8b)$$

The pre-factor of one-half in these expressions is assigned as approximately half of the top cell's photon flux is assumed to be emitted in the direction of the bottom cell, and vice versa, as illustrated in Fig. 2(a). We note that, in principle, the radiative couplings between the cells can be influenced by the refractive indices of the cells and any additional layers between them, including transport layers and electrodes.⁵⁷ In addition, the angular-range of emission is limited by the refractive indices of the respective layers, with total internal reflection leading to some reduction in the radiative coupling factors.^{9,13,66} Equation (8) therefore provides a reasonable upper estimate on the radiative couplings in the thermodynamic limit, which are likely to be lower in practice.

As the cells of the two-junction device can be connected independently or serially, Eqs. (5)–(8) may be solved in two ways. In this work, we focus on the serially connected or “two-terminal” case, with the independently connected or “four-terminal” case being considered in [supplementary material](#) (Note 7). In the two-terminal case, the total current density J produced under applied voltage bias V satisfies $J_1(V_1) = J_2(V_2) \equiv J(V)$, as per Kirchhoff's current

law, while the voltage drops across each cell satisfy $V_1 + V_2 = V$. Of course, the radiative couplings described in Eqs. (7) and (8) will influence these current densities, although these are assumed to be a second-order contribution that can be incorporated via an iterative loop. For a given voltage (V), the total current density (J) can be determined by iteratively solving Eqs. (5)–(8) using the process illustrated in Fig. 2(b), where radiative coupling is assumed negligible in the first iteration ($V_{em,1} \approx 0$ and $V_{em,2} \approx 0$), and the current densities are equated to deduce V_1 . This voltage is used to evaluate the current density (J), which in turn is used to evaluate each cell's emission voltage in the dark ($V_{em,1}$ and $V_{em,2}$; see [supplementary material](#) - Note 8), so the process is repeated until the absolute change in current density between iterations is smaller than some convergence criterion, ξ . In this work, we took $\xi = 10^{-6}$ to ensure six significant figure precision in the simulation result, allowing us to draw conclusions while minimizing numerical inaccuracies arising from a nonconvergent iterative process.

By varying the voltage, V , and determining the resultant current density, J , produced by the multi-junction device using this iterative process, performance metrics of any combination of cells can be determined while also accounting for realistic radiative couplings between them. We note that this analysis can be utilized for both ideal direct bandgaps in the SQ model and experimentally determined EQEPV spectra, although Eqs. (5)–(8) simplify greatly in the SQ model, as described in the [supplementary material](#) (Note 6), with the effects of band-filling becoming negligible for all voltages of interest.³⁷

C. Multi-junctions for indoor photovoltaic applications

Using the general approach described in Sec. II B, the thermodynamic performance limits of multi-junction PV devices were simulated under indoor illumination conditions by assuming LED-B4 at 1000 lux as a light source. First, the PCE was calculated in the idealized SQ model as a function of the top cell's bandgap ($E_{g,1}$) and the bottom cell's bandgap ($E_{g,2}$). In the SQ model, the shunt resistance of both devices is assumed infinite, with $R_{sh,1} \rightarrow \infty$ and $R_{sh,2} \rightarrow \infty$ in Eq. (5). The resultant PCEs were calculated with and without radiative couplings, with the results illustrated in Figs. 3(a) and 3(b), respectively. Complementary figures considering the maximum power point voltage (V_{mpp}) and current density (J_{mpp}) are provided as [supplementary material](#) (Note 6). We find that a maximum PCE of around 61% is obtained in the case without radiative coupling, which increases to 77% when radiative couplings between both cells are incorporated. In both cases, the optimal bandgap configuration is $E_{g,1} \sim 2.2$ eV and $E_{g,2} \sim 1.7$ eV. Interestingly, a wide-gap top cell with $E_{g,1} \sim 2.1$ eV could be combined with any narrow-gap bottom cell with $E_{g,2}$ between 1.0 and 2.0 eV to yield a PCE in excess of 60%, with many semiconductor materials possessing bandgaps in this range. In other words, high-efficiency indoor multi-junction PVs can be realized by coupling a suitably selected wide-gap top cell with a bottom cell based on almost any state-of-the-art material optimized under AM1.5 G conditions. This is a new insight and not necessarily intuitive.

To showcase the relevance of our approach for modeling multi-junction PVs, we simulated the performance of several perovskite–perovskite and perovskite–inorganic combinations

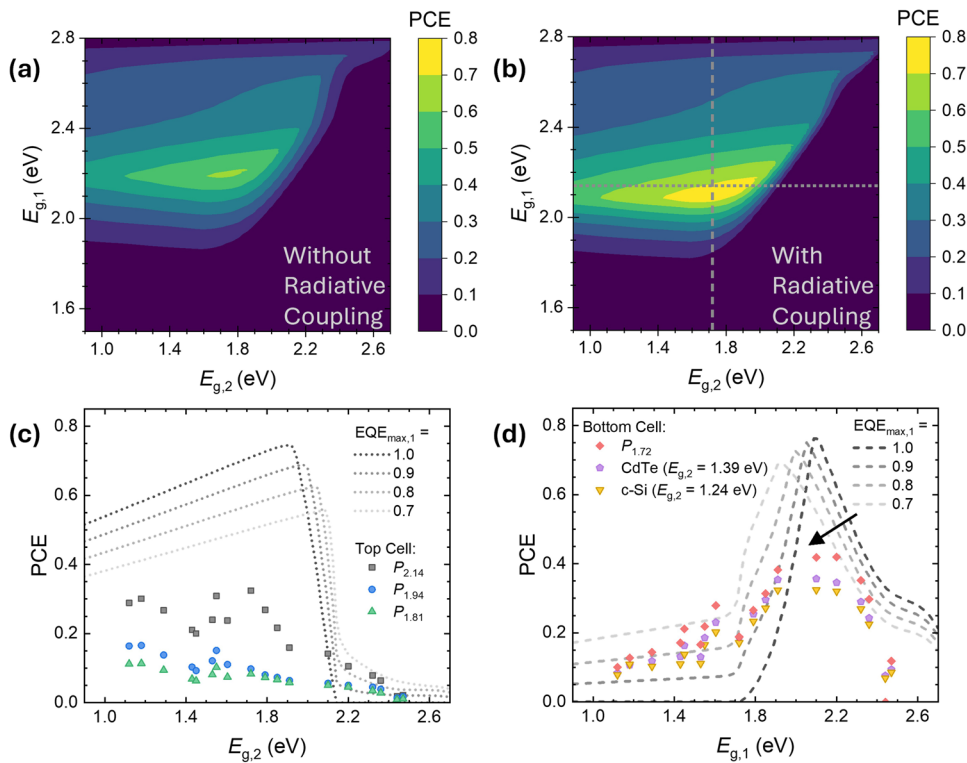


FIG. 3. Optimal bandgap configurations for multi-junction PVs under LED-B4 illumination (at an illuminance of 1000 lux). (a) Without and (b) with radiative couplings between cells, power conversion efficiencies are plotted in the SQ model as a function of top cell bandgap ($E_{g,1}$) and bottom cell bandgap ($E_{g,2}$), giving a peak efficiency of around 77% at $E_{g,1} \sim 2.2$ eV and $E_{g,2} \sim 1.7$ eV. The dotted horizontal line and dashed vertical line indicate slices made for fixed $E_{g,1}$ /varied $E_{g,2}$ and vice versa, respectively, which correspond to the widest-gap systems considered in (c) and (d). In (c), the top cell has been fixed and the bottom cell is varied, while in (d), the bottom cell is fixed and the top cell is varied. For reference, the PCE has been simulated in a modified SQ model (using a variety of top cell $\text{EQE}_{\text{max},1}$) with fixed $E_{g,1} = 2.14$ eV in (c) and with fixed $E_{g,2} = 1.72$ eV in (d).

using their experimentally determined EQE_{PV} spectra and V_{oc}^{\odot} measurements. These spectra need not be as sensitive as the EQE_{PV} spectrum for the DCP device considered in Fig. 1(a)—a couple of orders of magnitude below saturation is usually sufficient. Note that the combinations considered in this investigation are not fully optimized; they do, however, illustrate how the large library of materials optimized under solar conditions can be reconsidered for indoor applications. Herein, the various perovskite systems are labeled according to their bandgap (E_g) in electronvolts as P_{E_g} (see [supplementary material](#) - Note 9 for all material details and EQE_{PV} spectra). Figure 3(c) shows the resultant multi-junction PCEs for various perovskite-perovskite devices, where perovskite top cells with 1.81,⁶⁷ 1.94,⁶⁸ and 2.14 eV⁶⁹ bandgaps were combined with a variety of perovskite bottom cells.^{56,70–82} Note that the shunt resistance of each cell in the multi-junction device is assumed infinite in these thermodynamic limit calculations; we explore the effect of parasitic resistances in Sec. II E. As predicted from Figs. 3(a) and 3(b), a wide range of bottom cell bandgaps can perform well for a given top cell material. For example, $P_{2.14}$ exhibits a PCE of around 27% with both $P_{1.29}$ and $P_{1.79}$. On the other hand, when the top cell has a narrower bandgap than the bottom cell, the PCE of the multi-junction device drops to near-zero due to reduced photocurrent generation in the latter.

Similarly, Fig. 3(d) illustrates the resultant PCE when the bottom cell material was fixed while the top cell material was varied. In this case, one perovskite and two inorganic bottom cells were used, namely, a crystalline-silicon (c-Si) device with $E_{g,2} \approx 1.24$ eV,⁸³ a selenium-doped CdTe device with $E_{g,2} \approx 1.39$ eV,⁸⁴ and a

perovskite device with $E_{g,2} = 1.72$ eV.⁸⁵ As expected, high-performance multi-junctions can be achieved using bottom cells with fairly narrow bandgaps. In all cases, the optimal top cell has a bandgap $E_{g,1} \sim 2.1$ eV, with the PCE decreasing either side of this maximum. Upon studying Fig. 3 carefully, it becomes apparent that some of the PCEs evaluated using experimentally determined EQE_{PV} spectra seemingly surpass the limits predicted by the SQ model. This, however, is a consequence of the top cell's above-gap EQE_{PV} being less than unity for most of the perovskites (see [supplementary material](#) - Note 9). As the model assumes a near-unity IQE, the surplus high energy light that is not absorbed by the top cell gets transmitted through to the bottom cell. This effect is explored in Fig. 3 by reducing the top junction's above-gap EQE_{PV} from $\text{EQE}_{\text{max}} = 1$ to $\text{EQE}_{\text{max}} = 0.7$, with the results illustrated for a fixed $E_{g,1} = 2.14$ eV top cell by the dotted curves in Fig. 3(c) and for a fixed $E_{g,2} = 1.72$ eV bottom cell by the dashed curves in Fig. 3(d). From these curves—which correspond to horizontal and vertical sweeps across Fig. 3(b), respectively—it is clear that a reduction (increase) in the top cell's absorbance (transmittance) can relax restrictions on the bottom cell's bandgap, enabling higher performance for some bandgap combinations than predicted by the SQ model.

From Fig. 3, it is clear that multi-junction approaches can generate more power than single junctions, provided that the bandgap and absorbances of each cell are optimized to achieve suitable current matching. This, however, is a non-trivial process that closely depends on the selected materials. While all combinations presented in Figs. 3(c) and 3(d) offer higher V_{mpp} values than obtainable by

single cells—which is ideal for indoor PV applications—this does not always translate to high power generation (see [supplementary material](#) - Note 10). Generally, multi-junction approaches offer higher PCEs when $E_{g,1} \approx 2.1$ eV and $E_{g,2}$ lies between 1.0 and 1.8 eV. It is important to note, however, that as indoor PVs are often used in energy-harvesting systems that employ a harvest-store-use architecture,⁸⁶ where energy is stored in a supercapacitor or battery by an intermediary energy-harvesting board, then the voltage generated by the PV device is a key design parameter.⁸⁷

D. Sensitivity to changes in light source

In the analyses presented so far, LED-B4 illumination has been assumed to comply with indoor PV testing standard IEC TS 62607-7-2:2023.^{51,52} While testing standards are vital for reliable intercomparisons between laboratories and research groups, alongside the accurate verification of commercial product performance, the use of a single spectrum does not capture the diverse range of light sources that will be found in many indoor settings, with LEDs, fluorescent (FL) lamps, or even some combination of artificial light and daylight being commonly found.⁸⁸ For this reason, we considered the performance of some of the optimized multi-junction devices discussed in [Figs. 3\(c\) and 3\(d\)](#) under a variety of light sources commonly found in indoor settings. [Figure 4](#) shows the PCE, V_{mpp} , and maximum power point current density (J_{mpp}) of selected cells under a variety of indoor light sources (with each having an irradiance of $0.3132 \text{ mW cm}^{-2}$, corresponding to an illuminance of 1000 lux under LED-B4 illumination). In addition, the performance of the devices is also considered under the AM0, AM1, and AM1.5 G photon fluxes at their usual irradiances. The LED-B4 spectrum that the multi-junction combinations were optimized under is indicated by the vertical dashed lines, with a color temperature approximating that of a 5000 K LED. For reference, the performance of a single junction device in the SQ model was also simulated using the optimal bandgap (under LED-B4 illumination) of $E_g = 1.83$ eV, with the results plotted as stars connected by dotted lines.

Generally, the PCE [[Fig. 4\(a\)](#)] of the multi-junction devices is more sensitive to changes in light source, with these variations predominantly being due to variations in photocurrent generation and radiative coupling with light source, as illustrated by the changes in J_{mpp} [[Fig. 4\(b\)](#)]. On the other hand, V_{mpp} [[Fig. 4\(c\)](#)] is more robust, changing by less than 100 mV for the considered indoor light sources. This is an important observation as the voltage output by the indoor PV device will be similar under many different sources of artificial light, not just the light source specified in a test standard. Moreover, the V_{mpp} of all the multi-junction devices (which are not fully optimized) surpasses that of the single-junction device under all light sources, meaning that multi-junction PVs can provide a larger potential difference than single junctions under indoor lighting conditions, making them more desirable for energy harvesting, remote sensing, and other Internet-of-things applications.^{87,90}

E. Effect of parasitic resistances and changes in light intensity

In the preceding discussions, parasitic resistances were assumed negligible. However, at the low-light intensities typical of indoor environments, a low shunt resistance can severely impact device performance, while the series resistance has little effect.⁵⁵

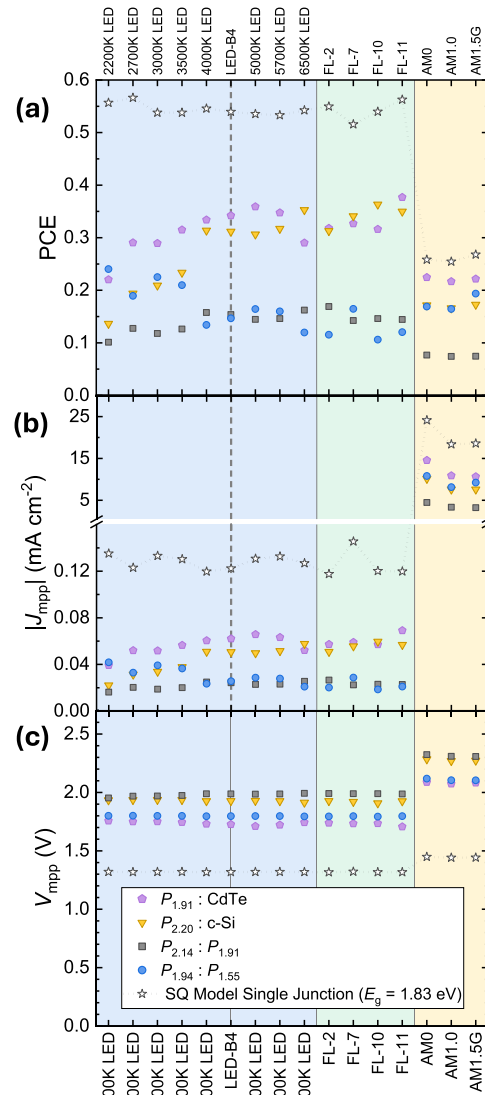


FIG. 4. Probing the sensitivity of (a) the PCE, (b) the absolute value of the maximum power point current density (J_{mpp}), and (c) the V_{mpp} of a few exemplary multi-junction combinations to changes in light source. Note that an irradiance of $0.3132 \text{ mW cm}^{-2}$ was used for the LED and fluorescent (FL) sources (corresponding to an illuminance of 1000 lux under LED-B4), while the solar spectra hold their usual intensities, which are AM0: 135.3 mW cm^{-2} ; AM1: 104 mW cm^{-2} ; and AM1.5 G: 100 mW cm^{-2} . The photon fluxes of the considered light sources are available in the [supplementary material](#) (Note 3).⁸⁹ Note that the LED-B4 light source under which the multi-junction devices were optimized is indicated by the vertical dashed line.

Alternatively, at the high intensities typical of solar cell operating conditions, a high series resistance (including the sheet resistance of any transparent electrodes) will instead lead to losses in device performance.^{91,92} To demonstrate how the simulation approach described in this work can consider both extremes of operating conditions while incorporating parasitic resistances, the performance

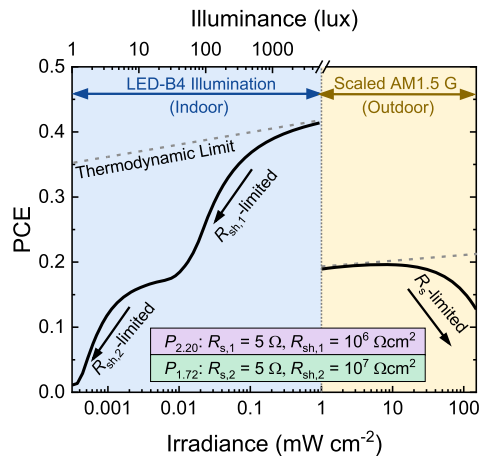


FIG. 5. Applying the multi-junction simulation approach (including bidirectional radiative coupling) to a variety of lighting conditions while accounting for parasitic resistances. The power conversion efficiency (PCE) of a $P_{2,20}:P_{1,72}$ multi-junction device was simulated under LED-B4 illumination for irradiances $< 1 \text{ mW cm}^{-2}$ and under scaled AM1.5 G illumination for irradiances $> 1 \text{ mW cm}^{-2}$. The device has area $A = 10 \text{ cm}^2$, with both cells having series resistance $R_{s,1} = R_{s,2} = 5 \Omega$, whereas the top and bottom cells have shunt resistances $R_{sh,1} = 10^6 \Omega \text{ cm}^2$ and $R_{sh,2} = 10^7 \Omega \text{ cm}^2$, respectively. Note that the dashed lines indicate the thermodynamic limit, in which $R_{s,1} = R_{s,2} = 0$ and $R_{sh,1} = R_{sh,2} \rightarrow \infty$.

of a $P_{2,20}:P_{1,72}$ multi-junction device was simulated. In this analysis, the top and bottom cells were assumed to have shunt resistances $R_{sh,1} = 10^6 \Omega \text{ cm}^2$ and $R_{sh,2} = 10^7 \Omega \text{ cm}^2$, respectively. Both cells were assumed to have series resistance $R_{s,1} = R_{s,2} = 5 \Omega$, and cross-sectional area $A = 10 \text{ cm}^2$, with these resistances included as described in the [supplementary material](#) (Note 6). We note that the selected values are by no means optimal but were instead selected to illustrate how device performance becomes limited at different light intensities. The simulation results are plotted as a function of irradiance in [Fig. 5](#), where LED-B4 illumination is assumed for irradiances below 1 mW cm^{-2} (or 5000 lux), and scaled AM1.5 G illumination is assumed for irradiances above this value.

From the indoor light intensity (blue) region of [Fig. 5](#), it is clear that as the light intensity is reduced, the top cell first limits device performance due to its lower $R_{sh,1}$. As the irradiance is further decreased, the top cell acts as a photoresistor (see [supplementary material](#) - Note 11) and the PCE reduces to a value expected for the bottom cell under Φ_2 illumination. At irradiances below 0.001 mW cm^{-2} (or illuminances below 30 lux), the shunt resistance of the bottom cell dominates, ultimately causing the PCE to drop to zero. Alternatively, in the outdoor light intensity (yellow) region of [Fig. 5](#) (where scaled AM1.5 G illumination is used), the combined series resistance of the two cells leads to Ohmic losses that almost halve the PCE at one-sun irradiances (100 mW cm^{-2}) compared to the thermodynamic limit.

III. CONCLUSION

To conclude, we have presented an approach for optimizing the design of multi-junction PVs while accounting for intrinsic processes in real devices, including sub-gap absorption, band-filling, non-radiative open-circuit voltage losses, and radiative couplings

between junctions. The approach uses each cell's experimental EQE_{PV} and $V_{\text{oc}}^{\text{oc}}$ measurements to predict absorption, emission, and transmission of light in the multi-junction device, enabling the evaluation of the PV figures-of-merit under any light source.

Using this approach, a case study was presented on the performance of perovskite-based multi-junctions for indoor PV applications. In the SQ model, optimal bandgap configurations were determined under LED-B4 illumination, with a wider-gap $E_{g,1} \sim 2.1 \text{ eV}$ and a narrow-gap $E_{g,2}$ between 1.0 and 2.0 eV , yielding PCEs higher than 60% . In other words, high-efficiency, high- V_{mpp} indoor PVs can be achieved by pairing a suitably selected wide-gap top cell with a bottom cell based on almost any conventional solar cell material. Moreover, by reducing the absorbance of the top cell to allow more high-energy light to be transmitted into the bottom cell, it was found that moderate performance could be achieved for combinations of bandgaps that are deemed poor by the SQ model.

Following this, optimal configurations of real PV materials for high-performance multi-junctions were identified using their experimentally determined EQE_{PV} spectra and inferred EQE_{EL} values. The sensitivity of these optimized devices to changes in illumination conditions was probed by considering their performance under a variety of light sources and intensities commonly found indoors, thus paving the way from optimization under testing standard conditions to versatility in real-world deployment locations. It was found that the PCE and J_{mpp} are more sensitive to changes in light source, while V_{mpp} is a more robust metric, with non-optimized multi-junctions providing a larger V_{mpp} than can be generated by a single junction device.

Future techno-economic and life-cycle analyses employing the approach described in this work could consider many more combinations of the vast library of semiconductor materials to identify optimal systems for use under a broad variety of light sources, including, but not limited to, sources of artificial light, AM1.5 G illumination, and even AM0 illumination for space applications. These investigations need not be limited to one type of photovoltaic material and could compare the power output of inorganic, perovskite, and organic photovoltaics alongside other metrics such as cost, material risk (e.g., lead in perovskites), embodied energy vs longevity, and more. Future enhancements that could be made to the tool include adding spectrally dependent and angularly dependent reflections between cells, which could improve the accuracy of the simulation approach at the cost of additional complexity and increased data requirements (with the optical constants of each layer in the device being required).

SUPPLEMENTARY MATERIAL

Additional figures and notes are available as [supplementary material](#), including a list of symbols and abbreviations, the four-terminal limits of a multi-junction device under LED-B4 illumination, the scaling of the simulation approach to an arbitrary number of junctions, shunt-dependent simulations, and the EQE_{PV} spectra and $\Delta V_{\text{oc}}^{\text{nr}}$ values of all devices considered in this work.

ACKNOWLEDGMENTS

This work was funded by the UKRI through the EPSRC Program Grant No. EP/T028513/1 *Application Targeted and Integrated*

Photovoltaics and the UKRI Research England RPIF Programme (Center for Integrative Semiconductor Materials). This work was also supported through the Welsh Government's Sêr Cymru II Program "Sustainable Advanced Materials" (Welsh European Funding Office—European Regional Development Fund). P.M. is a Sêr Cymru II Research Chair.

AUTHOR DECLARATIONS

Conflict of Interest

The authors have no conflicts to disclose.

Author Contributions

Austin M. Kay: Conceptualization (equal); Data curation (lead); Formal analysis (equal); Investigation (equal); Methodology (equal); Resources (lead); Software (lead); Validation (equal); Visualization (equal); Writing – original draft (lead); Writing – review & editing (equal). **Drew B. Riley:** Conceptualization (equal); Data curation (equal); Formal analysis (equal); Investigation (equal); Methodology (equal); Resources (equal); Software (lead); Supervision (equal); Validation (equal); Visualization (equal); Writing – original draft (equal); Writing – review & editing (equal). **Gregory Burwell:** Conceptualization (equal); Data curation (equal); Formal analysis (equal); Investigation (equal); Methodology (equal); Resources (equal); Supervision (equal); Visualization (equal); Writing – original draft (equal); Writing – review & editing (equal). **Paul Meredith:** Conceptualization (equal); Formal analysis (equal); Funding acquisition (lead); Investigation (equal); Methodology (equal); Project administration (lead); Supervision (equal); Visualization (equal); Writing – review & editing (equal).

DATA AVAILABILITY

The data and computational tool used to simulate the findings in this work are available online.⁴⁶ The data used to create the figures are available at <https://github.com/Austin-M-Kay/Data>.

REFERENCES

- J. A. Nelson, *The Physics of Solar Cells* (Imperial College Press, 2003).
- L. C. Hirst and N. J. Ekins-Daukes, "Fundamental losses in solar cells," *Prog. Photovoltaics: Res. Appl.* **19**(3), 286–293 (2011).
- C. H. Henry, "Limiting efficiencies of ideal single and multiple energy gap terrestrial solar cells," *J. Appl. Phys.* **51**(8), 4494–4500 (1980).
- A. Yakimov and S. R. Forrest, "High photovoltage multiple-heterojunction organic solar cells incorporating interfacial metallic nanoclusters," *Appl. Phys. Lett.* **80**(9), 1667–1669 (2002).
- M. Bonnet-Eymard *et al.*, "Optimized short-circuit current mismatch in multi-junction solar cells," *Sol. Energy Mater. Sol. Cells* **117**, 120–125 (2013).
- E. Lopez *et al.*, "Experimental coupling process efficiency and benefits of back surface reflectors in photovoltaic multi-junction photonic power converters," *Prog. Photovoltaics: Res. Appl.* **29**(4), 461–470 (2021).
- R. Strandberg, "An analytic approach to the modeling of multijunction solar cells," *IEEE J. Photovoltaics* **10**(6), 1701–1711 (2020).
- H. Ferhati, F. Djeflal, and L. B. Drissi, "A new approach to the modeling and simulation of multi-junction solar cells," *Optik* **200**, 163452 (2020).
- A. Martí and G. L. Araújo, "Limiting efficiencies for photovoltaic energy conversion in multigap systems," *Sol. Energy Mater. Sol. Cells* **43**(2), 203–222 (1996).
- R. Santbergen *et al.*, "GenPro4 optical model for solar cell simulation and its application to multijunction solar cells," *IEEE J. Photovoltaics* **7**(3), 919–926 (2017).
- M. Babar *et al.*, "Analytical model of multi-junction solar cell," *Arabian J. Sci. Eng.* **39**(1), 547–555 (2014).
- M. Hermle *et al.*, "Numerical simulation of tunnel diodes for multi-junction solar cells," *Prog. Photovoltaics: Res. Appl.* **16**(5), 409–418 (2008).
- D. Alonso-Álvarez *et al.*, "Solcore: A multi-scale, Python-based library for modelling solar cells and semiconductor materials," *J. Comput. Electron.* **17**, 1099–1123 (2018).
- U. Aeberhard *et al.*, "Analysis and optimization of organic tandem solar cells by full opto-electronic simulation," *Front. Photonics* **3**, 891565 (2022).
- See <https://www.fluxim.com/setfos-intro> for SETFOS by FLUXIM AG; accessed 10 November 2024.
- A. Kowsar *et al.*, "Comparative study on solar cell simulators," in *2019 2nd International Conference on Innovation in Engineering and Technology (ICIET)* (IEEE, 2019).
- C. R. Lewis *et al.*, "Recent developments in multijunction solar cell research," *Sol. Cells* **24**(1–2), 171–183 (1988).
- H. F. Macmillan *et al.*, "Recent advances in multi-junction III–V solar cell development," *Sol. Cells* **27**(1–4), 205–217 (1989).
- J. Nelson *et al.*, "Observation of suppressed radiative recombination in single quantum well p-i-n photodiodes," *J. Appl. Phys.* **82**(12), 6240–6246 (1997).
- M. B. Spitzer and J. C. C. Fan, "Multijunction cells for space applications," *Sol. Cells* **29**(2–3), 183–203 (1990).
- J. P. Connolly *et al.*, "Designing III–V multijunction solar cells on silicon," *Prog. Photovoltaics: Res. Appl.* **22**(7), 810–820 (2014).
- S. P. Philipps, F. Dimroth, and A. W. Bett, "Chapter I-4-B–High-efficiency III–V multijunction solar cells," in *McEvoy's Handbook of Photovoltaics*, 3rd ed., edited by S. A. Kalogirou (Academic Press, 2018), pp. 439–472.
- J. Li *et al.*, "A brief review of high efficiency III–V solar cells for space application," *Front. Phys.* **8**, 631925 (2021).
- A. R. Bowman *et al.*, "Relaxed current matching requirements in highly luminescent perovskite tandem solar cells and their fundamental efficiency limits," *ACS Energy Lett.* **6**(2), 612–620 (2021).
- M. T. Hörantner-Leijtens *et al.*, "The potential of multijunction perovskite solar cells," *ACS Energy Lett.* **2**(10), 2506–2513 (2017).
- D. P. McMeekin *et al.*, "Solution-processed all-perovskite multi-junction solar cells," *Joule* **3**(2), 387–401 (2019).
- F. Urbach, "The long-wavelength edge of photographic sensitivity and of the electronic absorption of solids," *Phys. Rev.* **92**(5), 1324 (1953).
- E. Ugur *et al.*, "Life on the Urbach edge," *J. Phys. Chem. Lett.* **13**(33), 7702–7711 (2022).
- N. Zarrabi *et al.*, "Charge-generating mid-gap trap states define the thermodynamic limit of organic photovoltaic devices," *Nat. Commun.* **11**(1), 5567 (2020).
- G. J. W. Aalbers *et al.*, "Effect of sub-bandgap defects on radiative and non-radiative open-circuit voltage losses in perovskite solar cells," *Nat. Commun.* **15**(1), 1276 (2024).
- S. Zeiske *et al.*, "Static disorder in lead halide perovskites," *J. Phys. Chem. Lett.* **13**(31), 7280–7285 (2022).
- C. Kaiser *et al.*, "A universal Urbach rule for disordered organic semiconductors," *Nat. Commun.* **12**(1), 3988 (2021).
- X. Wu *et al.*, "Trap states in lead iodide perovskites," *J. Am. Chem. Soc.* **137**(5), 2089–2096 (2015).
- J. Chantana *et al.*, "Impact of Urbach energy on open-circuit voltage deficit of thin-film solar cells," *Sol. Energy Mater. Sol. Cells* **210**, 110502 (2020).
- M. Li, P. Huang, and H. Zhong, "Current understanding of band-edge properties of halide perovskites: Urbach tail, rashba splitting, and exciton binding energy," *J. Phys. Chem. Lett.* **14**(6), 1592–1603 (2023).
- P. Ščájev *et al.*, "Impact of dopant-induced band tails on optical spectra, charge carrier transport, and dynamics in single-crystal CdTe," *Sci. Rep.* **12**(1), 12851 (2022).
- A. M. Kay *et al.*, "The thermodynamic limit of indoor photovoltaics based on energetically-disordered molecular semiconductors," *Sol. RRL* **7**, 2300277 (2023).

- ³⁸J. Wong, S. T. Omelchenko, and H. A. Atwater, "Impact of semiconductor band tails and band filling on photovoltaic efficiency limits," *ACS Energy Lett.* **6**(1), 52–57 (2020).
- ³⁹Y. Cheng *et al.*, "Revealing the degradation and self-healing mechanisms in perovskite solar cells by sub-bandgap external quantum efficiency spectroscopy," *Adv. Mater.* **33**(3), 2006170 (2021).
- ⁴⁰S. Zeiske *et al.*, "Sensitivity of sub-bandgap external quantum efficiency measurements of solar cells under electrical and light bias," *ACS Photonics* **7**(1), 256–264 (2020).
- ⁴¹B. T. van Gorkom *et al.*, "Revealing defective interfaces in perovskite solar cells from highly sensitive sub-bandgap photocurrent spectroscopy using optical cavities," *Nat. Commun.* **13**(1), 349 (2022).
- ⁴²K. Vandewal *et al.*, "Fourier-transform photocurrent spectroscopy for a fast and highly sensitive spectral characterization of organic and hybrid solar cells," *Thin Solid Films* **516**(20), 7135–7138 (2008).
- ⁴³A. Vlk *et al.*, "Spatial localization of defects in halide perovskites using photothermal deflection spectroscopy," *J. Phys. Chem. Lett.* **15**(5), 1273–1278 (2024).
- ⁴⁴G. Longo *et al.*, "Understanding the performance-limiting factors of $\text{Cs}_2\text{AgBiBr}_6$ double-perovskite solar cells," *ACS Energy Lett.* **5**(7), 2200–2207 (2020).
- ⁴⁵B. Subedi *et al.*, "Effects of intrinsic and atmospherically induced defects in narrow bandgap $(\text{FASnI}_3)_x(\text{MAPbI}_3)_{1-x}$ perovskite films and solar cells," *J. Chem. Phys.* **152**(6), 064705 (2020).
- ⁴⁶A. M. Kay (2025). "Photovoltaic performance simulator (PV-simulator)," GitHub. https://github.com/Austin-M-Kay/Photovoltaic_Performance_Simulator
- ⁴⁷O. Almora *et al.*, "Device performance of emerging photovoltaic materials (version 3)," *Adv. Energy Mater.* **13**(1), 2203313 (2023).
- ⁴⁸T. J. Jacobsson *et al.*, "An open-access database and analysis tool for perovskite solar cells based on the FAIR data principles," *Nat. Energy* **7**(1), 107–115 (2021).
- ⁴⁹G. Burwell *et al.*, "Wide-gap perovskites for indoor photovoltaics," *Sol. RRL* **8**, 2400180 (2024).
- ⁵⁰K.-L. Wang *et al.*, "Perovskite indoor photovoltaics: Opportunity and challenges," *Chem. Sci.* **12**(36), 11936–11954 (2021).
- ⁵¹International Electrotechnical Commission, Indoor Testing Standard 62607-7-2:2023, available at: <https://webstore.iec.ch/publication/61819>.
- ⁵²D. E. Parsons, G. Koutsourakis, and J. C. Blakesley, "Performance measurements for indoor photovoltaic devices: Classification of a novel light source," *APL Energy* **2**(1), 016110 (2024).
- ⁵³U. Rau, "Reciprocity relation between photovoltaic quantum efficiency and electroluminescent emission of solar cells," *Phys. Rev. B* **76**(8), 085303 (2007).
- ⁵⁴P. Würfel, "The chemical potential of radiation," *J. Phys. C: Solid State Phys.* **15**(18), 3967 (1982).
- ⁵⁵G. Burwell *et al.*, "Scaling considerations for organic photovoltaics for indoor applications," *Sol. RRL* **6**(7), 2200315 (2022).
- ⁵⁶M. Othman *et al.*, "Alleviating nanostructural phase impurities enhances the optoelectronic properties, device performance and stability of cesium-formamidinium metal-halide perovskites," *Energy Environ. Sci.* **17**(11), 3832–3847 (2024).
- ⁵⁷L. A. A. Pettersson, L. S. Roman, and O. Inganäs, "Modeling photocurrent action spectra of photovoltaic devices based on organic thin films," *J. Appl. Phys.* **86**(1), 487–496 (1999).
- ⁵⁸A. Armin *et al.*, "Limitations of charge transfer state parameterization using photovoltaic external quantum efficiency," *Adv. Energy Mater.* **10**(41), 2001828 (2020).
- ⁵⁹A. M. Kay *et al.*, "Quantifying the excitonic static disorder in organic semiconductors," *Adv. Funct. Mater.* **32**(32), 2113181 (2022).
- ⁶⁰G. K. Grandhi *et al.*, "Promises and challenges of indoor photovoltaics," *Nat. Rev. Clean Technol.* **1**(2), 132–147 (2025).
- ⁶¹S. M. Sze, Y. Li, and K. K. Ng, *Physics of Semiconductor Devices*, 4th ed. (John Wiley & Sons, Inc., Hoboken, NJ, 2021).
- ⁶²W. Shockley and H. J. Queisser, "Detailed balance limit of efficiency of p - n junction solar cells," *J. Appl. Phys.* **32**(3), 510–519 (1961).
- ⁶³D. Lübke *et al.*, "Comparing and quantifying indoor performance of organic solar cells," *Adv. Energy Mater.* **11**(34), 2101474 (2021).
- ⁶⁴M. Freunek, M. Freunek, and L. M. Reindl, "Maximum efficiencies of indoor photovoltaic devices," *IEEE J. Photovoltaics* **3**(1), 59–64 (2013).
- ⁶⁵D. Müller *et al.*, "Indoor photovoltaics for the internet-of-things—A comparison of state-of-the-art devices from different photovoltaic technologies," *ACS Appl. Energy Mater.* **6**(20), 10404–10414 (2023).
- ⁶⁶J. Nelson *et al.*, "Effect of quantum well location on single quantum well p - i - n photodiode dark currents," *J. Appl. Phys.* **86**(10), 5898–5905 (1999).
- ⁶⁷J. Wang *et al.*, "Highly efficient all-inorganic perovskite solar cells with suppressed non-radiative recombination by a Lewis base," *Nat. Commun.* **11**(1), 177 (2020).
- ⁶⁸W. Chen *et al.*, "Surface reconstruction for stable monolithic all-inorganic perovskite/organic tandem solar cells with over 21% efficiency," *Adv. Funct. Mater.* **32**(5), 2109321 (2022).
- ⁶⁹W. Zhu *et al.*, "Aged precursor solution toward low-temperature fabrication of efficient carbon-based all-inorganic planar CsPbI_2Br perovskite solar cells," *ACS Appl. Energy Mater.* **1**(9), 4991–4997 (2018).
- ⁷⁰X. Zhou *et al.*, "Integrated ideal-bandgap perovskite/bulk-heterojunction solar cells with efficiencies > 24%," *Adv. Mater.* **34**(40), 2205809 (2022).
- ⁷¹Y. Lei *et al.*, "Perovskite superlattices with efficient carrier dynamics," *Nature* **608**(7922), 317–323 (2022).
- ⁷²J. Yuan *et al.*, "Two-dimensional perovskite capping layer for stable and efficient tin-lead perovskite solar cells," *Sci. China Chem.* **62**(5), 629–636 (2019).
- ⁷³E. Joker *et al.*, "Robust tin-based perovskite solar cells with hybrid organic cations to attain efficiency approaching 10%," *Adv. Mater.* **31**(2), 1804835 (2019).
- ⁷⁴J.-h. Chen *et al.*, "Improved photovoltaic performance from high quality perovskite thin film grown with the assistance of PC_{71}BM ," *Chin. J. Polym. Sci.* **35**(2), 309–316 (2017).
- ⁷⁵Y. Zhou *et al.*, "Composition-tuned wide bandgap perovskites: From grain engineering to stability and performance improvement," *Adv. Funct. Mater.* **28**(35), 1803130 (2018).
- ⁷⁶W. Zhu *et al.*, "Band alignment engineering towards high efficiency carbon-based inorganic planar CsPbI_2Br perovskite solar cells," *ChemSusChem* **12**(10), 2318–2325 (2019).
- ⁷⁷H. Xu *et al.*, "Guanidinium-assisted crystallization modulation and reduction of open-circuit voltage deficit for efficient planar FAPbBr_3 perovskite solar cells," *Chem. Eng. J.* **437**, 135181 (2022).
- ⁷⁸X. Hu *et al.*, "Wide-bandgap perovskite solar cells with large open-circuit voltage of 1653 mV through interfacial engineering," *Sol. RRL* **2**(8), 1800083 (2018).
- ⁷⁹H. Yuan *et al.*, "All-inorganic CsPbBr_3 perovskite solar cell with 10.26% efficiency by spectra engineering," *J. Mater. Chem. A* **6**(47), 24324–24329 (2018).
- ⁸⁰L. Zuo *et al.*, "Highly efficient semitransparent solar cells with selective absorption and tandem architecture," *Adv. Mater.* **31**(36), 1901683 (2019).
- ⁸¹B. Li *et al.*, "Efficient and stable $\text{Cs}_2\text{AgBiBr}_6$ double perovskite solar cells through in-situ surface modulation," *Chem. Eng. J.* **446**, 137144 (2022).
- ⁸²X. Meng *et al.*, "Highly reproducible and efficient FASnI_3 perovskite solar cells fabricated with volatilizable reducing solvent," *J. Phys. Chem. Lett.* **11**(8), 2965–2971 (2020).
- ⁸³M. A. Green *et al.*, "Solar cell efficiency tables (Version 61)," *Prog. Photovoltaics: Res Appl.* **31**, 3 (2023).
- ⁸⁴R. Mallick *et al.*, "Arsenic-doped CdSeTe solar cells achieve world record 22.3% efficiency," *IEEE J. Photovoltaics* **13**(4), 510–515 (2023).
- ⁸⁵Z. Liu *et al.*, "Interface optimization via fullerene blends enables open-circuit voltages of 1.35 V in $\text{CH}_3\text{NH}_3\text{Pb}(\text{I}_{0.8}\text{Br}_{0.2})_3$ solar cells," *Adv. Energy Mater.* **11**(16), 2003386 (2021).
- ⁸⁶V. Pecunia, L. G. Occhipinti, and R. L. Z. Hoyer, "Emerging indoor photovoltaic technologies for sustainable internet of things," *Adv. Energy Mater.* **11**(29), 2100698 (2021).
- ⁸⁷A. M. Kay *et al.*, "Optimising photovoltaic modules for indoor energy-harvesting systems," *J. Phys.: Energy* **7**(3), 035019 (2025).

⁸⁸K. Seunarine *et al.*, “Light power resource availability for energy harvesting photovoltaics for self-powered IoT,” *J. Phys.: Energy* **6**(1), 015018 (2024).

⁸⁹Cree-LED, Cree-LED X-Lamp (R) LEDs; accessed 10 November 2024, available at: <https://www.cree-led.com/products/leds/xlamp/>.

⁹⁰X. Hou *et al.*, “Indoor application of emerging photovoltaics—progress, challenges and perspectives,” *J. Mater. Chem. A* **8**(41), 21503–21525 (2020).

⁹¹G. Burwell *et al.*, “Parameterization of metallic grids on transparent conductive electrodes for the scaling of organic solar cells,” *Adv. Electron. Mater.* **7**(6), 2100192 (2021).

⁹²N. BurrIDGE *et al.*, “Application-targeted metal grid-enhanced transparent electrodes for organic photovoltaics,” *Adv. Electron. Mater.* **11**(3), 2400645 (2025).